

Cooperative concurrence of $4f$ and $3d$ flat bands in kagome heavy-fermion metal YbCr_6Ge_6

Wenxin Lv^{1,2,†}, Pengcheng Ma^{3,†}, Tianqi Wang³, Shangjie Tian^{4,1,2}, Ying Ma⁵, Shouguo Wang⁴,
Xiao Zhang^{5,*}, Zhonghao Liu^{3,*}, and Hechang Lei^{1,2,*}

¹*School of Physics and Beijing Key Laboratory of Optoelectronic Functional Materials & Micro-Nano Devices, Renmin University of China, Beijing 100872, China*

²*Key Laboratory of Quantum State Construction and Manipulation (Ministry of Education), Renmin University of China, Beijing 100872, China*

³*Institute of High-Pressure Physics and School of Physical Science and Technology, Ningbo University, Ningbo 315211, China*

⁴*School of Materials Science and Engineering, Anhui University, Hefei 230601, China*

⁵*State Key Laboratory of Information Photonics and Optical Communications & School of Physical Science and Technology, Beijing University of Posts and Telecommunications, Beijing 100876, China*

†These authors contributed equally to this work.

*Corresponding authors: Z.X. (zhangxiaobupt@bupt.edu.cn); Z.H.L. (liuzhonghao@nbu.edu.cn);
H.C.L. (hlei@ruc.edu.cn)

Flat-band (FB) systems originating from special lattice geometry like in kagome metals as well as localized orbitals in the materials such as heavy-fermion (HF) compounds have induced intensive interest due to their band topology and strong electron correlation effects, leading to emergent quantum states of matter. However, the question of how these two distinct FBs coexist and interact remains unsettled. Here, we report that YbCr_6Ge_6 hosting both Cr-kagome lattice and Yb-4*f* electrons exhibits HF behaviors and a robust antiferromagnetic ground state with transition temperature $T_N = 3$ K, significantly higher than other similar kagome metals with Yb ions. Angle-resolved photoemission spectroscopy measurements reveal the coexistence of FBs originating from both Cr-kagome lattice and localized Yb-4*f* electrons near Fermi energy level E_F . More importantly, the clear spectroscopic signatures of a hybridization of Yb-4*f* FB with kagome-lattice-derived conduction bands and the high density of states of Cr-kagome FB near E_F provide the underlying microscopic mechanisms of HF behaviors and enhanced antiferromagnetism in YbCr_6Ge_6 . Our findings demonstrate that the novel kagome HF metals can not only host the cooperative coexistence of two different types of FBs, but also provide a paradigm material platform to explore the exotic correlated topological quantum phenomena.

The exploration of novel quantum states of matter is one of central topics in condensed matter physics. The systems with flat bands (FBs) emerge as a particularly fertile ground because the FBs not only suppress the electronic kinetic energy dramatically and enhance electron correlations significantly, but also process the nontrivial band topology ¹. The FBs can drive electronic systems towards a variety of strongly correlated states, including ferromagnetism, unconventional super-

conductivity and fractional Chern insulators ²⁻⁴. To date, several conceptually distinct strategies have been employed to engineer such FBs.

The first paradigm is lattice-geometry-driven FBs, epitomized by the two-dimensional (2D) kagome lattice. Such kind of lattice composed of corner-sharing triangles inherently hosts a destructive interference of electron wavefunctions that leads to a FB in its single-particle electronic structure, accompanied by Dirac cones and van Hove singularities ^{5,6}. This unique electronic structure has rendered kagome metals like the T_mSn_n ($T = Mn, Fe, Co$), RET_6X_6 ($RE =$ rare-earth elements, $X = Ge, Sn$), and AV_3Sb_5 family ($A = K, Rb, Cs$) as celebrated systems for investigating the intricate interplay between magnetism, charge order, superconductivity and band topology ⁶⁻¹⁴. In these materials, the low-energy physics is primarily dictated by the quantum geometry of the lattice and the correlations among itinerant d -electrons. A second fundamentally different route to construct FBs is utilizing the many-body effects, which has been realized in heavy-fermion (HF) systems ¹⁵. In these materials, typically containing lanthanide or actinide elements, the hybridization between localized f -electrons and dispersive itinerant electrons—the Kondo effect—gives rise to narrow, correlation-induced HF FBs with resonance peak of density of states (DOS) at the Fermi energy level (E_F). These emergent HF FBs, directly visualized by angle-resolved photoemission spectroscopy (ARPES) ^{16,17}, don't originate from the lattice geometry but instead are pure manifestation of strong electron correlations, hosting heavy quasiparticles with effective masses up to a thousand times that of a free electron.

Despite the remarkable progress have made in these two parallel fields, the physics of lattice-

geometry-driven kagome FBs and electron-correlation-driven f -electron FBs have remained largely disconnected. This raises an unexplored question: what novel quantum phenomena would emerge when these two distinct types of FBs coexist and interact with each other in a single material? In this work, we carried out a detailed study on YbCr_6Ge_6 hosting both kagome lattice and Yb-4 f electrons, which is a paradigm system to answer the above question. YbCr_6Ge_6 exhibits an antiferromagnetic (AFM) ground state of Yb ions with transition temperature $T_N \sim 3$ K, which is much larger than that in YbV_6Sn_6 ¹⁸. In addition, it exhibits the HF features above T_N . ARPES results further confirm that the Yb-4 f FBs coexist with the Cr-3 d FB originating from the kagome lattice near the E_F in YbCr_6Ge_6 . The Kondo hybridization of Yb-4 f FBs with itinerant electrons leads to the HF behaviors while the high DOS of Cr-3 d FB enhances the T_N of AFM ground state.

Results

Structure and transport behaviors in YbCr_6Ge_6 . LnCr_6Ge_6 ($\text{Ln} = \text{Yb}$ and Lu) single crystals were grown by using Sn flux. The detailed structural and composition characterizations are shown in Supplementary Figure 1. LnCr_6Ge_6 has a hexagonal crystal structure (space group $P6/mmm$, No. 191)¹⁹. It consists of Ln-Ge layer with Ln triangle lattice and Cr-Ge-Ge-Ge-Cr slab with double Cr kagome lattice stacking along c axis alternatively, as shown in Figs. 1a and 1b. Figures 1c and 1d depict the temperature dependence of magnetic susceptibility $\chi(T)$ under the field of 1 T for $H \parallel c$ and $H \parallel ab$, respectively. The $\chi(T)$ curve shows obvious easy-axis anisotropy in the temperature range from 2 to 300 K. The $\chi_{ab}(T)$ curve exhibits a wide hump near 50 K before the quick increase at lower temperature. In contrast, the $\chi_c(T)$ curve doesn't show such anomaly. For

both field directions, the high-temperature $\chi(T)$ curves can be fitted well using the Curie-Weiss (CW) law, $\chi(T) = \chi_0 + C/(T - \theta)$, where C is Curie constant and θ is Weiss temperature. The linear behaviors of $(\chi(T) - \chi_0)^{-1}$ curves at high temperature (blue squares in Figs. 1c and 1d) also indicate the validation of CW law. From the fitted C , the calculated effective moment $\mu_{\text{eff},c}$ is 4.81(2) $\mu_{\text{B}}/\text{f.u.}$ and $\theta_c = -40.0(4)$ K for $H \parallel c$ and $\mu_{\text{eff},ab} = 5.18(6)$ $\mu_{\text{B}}/\text{f.u.}$ and $\theta_{ab} = -69.5(4)$ K for $H \parallel ab$. The fitted θ values for both field directions are negative, implying the AFM interactions in this material. Both values of μ_{eff} are larger than the theoretical value of Yb^{3+} ($\mu_{\text{eff}} = 4.54$ $\mu_{\text{B}}/\text{f.u.}$), suggesting the valent state of Yb at high temperature is mainly +3 and Cr ions may have local moments. In order to confirm this conjecture, we measured the $\chi(T)$ curves of LuCr_6Ge_6 (Supplementary Fig. 2). The fitted $\mu_{\text{eff},c}$ and $\mu_{\text{eff},ab}$ is 0.88(6) and 0.85(8) $\mu_{\text{B}}/\text{f.u.}$, respectively, when the θ_c and θ_{ab} are -40.4(8) and -57.8(9) K. It further indicates Cr ions should have local moments and AFM interactions. As shown in the insets of Figs. 1c and 1d, the $\chi_{ab}(T)$ curve shows a drop below 3 K at 0.01 T while the $\chi_c(T)$ curve only exhibits a kink at same field. It indicates that there is an AFM transition with spin direction along the ab plane in YbCr_6Ge_6 . With the increase of magnetic field, the drop/kink on $\chi(T)$ curve are suppressed gradually to lower temperature, confirming the nature of transition is AFM further.

As shown in Fig. 1e, the field-dependent magnetization $M(\mu_0 H)$ for $H \parallel c$ is much larger than that for $H \parallel ab$ at 2 K, which could be due to the spin canting along the c axis. Moreover, for $H \parallel c$, the $M(\mu_0 H)$ curve shows a linear increasing trend in the range from 0 to about 0.9 T, then gradually saturates and reaches 1.40 $\mu_{\text{B}}/\text{f.u.}$ at 7 T, which is much lower than the saturation magnetic moment of Yb^{3+} of 4.0 $\mu_{\text{B}}/\text{f.u.}$. It implies that there may be a magnetization plateau

phase in YbCr_6Ge_6 with Yb triangle lattice. When compared to LuCr_6Ge_6 , the ab -plane resistivity $\rho_{ab}(T)$ curve of YbCr_6Ge_6 shows a hump near 90 K and a fast decrease at around 3 K (Fig. 1f). The latter should be related to the suppression of spin disorder scattering below the AFM transition. The inset of Fig. 1f shows the difference in resistivity $\Delta\rho_{ab}(T) = \rho_{ab,\text{Yb}}(T) - \rho_{ab,\text{Lu}}(T)$ in order to estimate the contribution of $4f$ electrons. The $\Delta\rho_{ab}(T)$ displays a maximum at ~ 90 K while the low-temperature $\Delta\rho_{ab}(T)$ decreases remarkably in a magnetic field, suggesting that the resistivity hump of YbCr_6Ge_6 at high temperature could be due to the appearance of Kondo coherence.

For the specific heat results of YbCr_6Ge_6 and LuCr_6Ge_6 at zero field (Fig. 2a), both of them at high temperature are close to the Dulong-Petit limit ($3NR$, blue line), where N ($= 13$) is the atomic number and R ($= 8.314 \text{ J mol}^{-1} \text{ K}^{-1}$) is the ideal gas constant. For LuCr_6Ge_6 , the low-temperature specific heat can be fitted using the relation $C_p/T = \gamma + \beta T^2$, where γ is electronic specific heat coefficient and β is lattice specific heat coefficient. The fitted γ is $73.4(4) \text{ mJ mol}^{-1} \text{ K}^{-2}$ when the values of β are $0.24(1) \text{ mJ mol}^{-1} \text{ K}^{-4}$. Correspondingly, the calculated Debye temperature Θ_D is $475(6) \text{ K}$ using the relationship $\Theta_D = (\frac{12\pi^4 NR}{5\beta})^{1/3}$. The γ value of LuCr_6Ge_6 is much larger than that of LuV_6Sn_6 ($17.4 \text{ mJ mol}^{-1} \text{ K}^{-2}$)¹⁸, which is likely to reflect that the electrons in Cr-based kagome lattice have stronger correlation effects than that in V-based kagome lattice. Figure 2b displays the specific heat data of YbCr_6Ge_6 in different magnetic fields at the low-temperature region. The zero-field C_p/T curve shows an upward trend when $T < 8$ K and a λ -type peak appears at 3 K, indicating a long-range magnetic ordering state emerges. The ordering temperature is consistent with that determined from the $\chi(T)$ curves. For zero-field data, we fit the low-temperature specific heat from 9 K to 14 K. The obtained γ value is $203(8) \text{ mJ mol}^{-1}$

K^{-2} , significantly larger than that of LuCr_6Ge_6 . This large γ value suggests the HF feature of YbCr_6Ge_6 when $T > T_N$. When the magnetic field (≤ 1 T) is applied along the c -axis, the λ -type peak moves to lower temperatures continuously, reflecting the AFM feature of long-range ordering in YbCr_6Ge_6 . At field higher than 1 T, the λ -type peak turns into a broad peak, which moves to higher temperatures with increasing the field. Such behavior can be observed more clearly in the magnetic specific heat $C_m(T)$ data (Fig. 2c), which are obtained by subtracting the specific heat of non-magnetic analogue LuCr_6Ge_6 . The magnetic entropy $S_m(T)$ is calculated by integrating $C_m(T)$ (Fig. 2d). It is noteworthy that due to the experimental limitation where measurements only extend down to 2 K, the calculated $S_m(T)$ may be subject to an underestimation. It is found that the $S_m(T)$ value is about 25 % of $R\ln(2)$ at T_N . Then, it increases gradually and reaches a value of $R\ln(2)$ and $R\ln(4)$ at ~ 35 K and ~ 80 K, respectively. At $T > 100$ K, the $S_m(T)$ saturates to about $14 \text{ J mol}^{-1} \text{ K}^{-1}$, which is close to the value of $R\ln(6)$ ($\sim 14.9 \text{ J mol}^{-1} \text{ K}^{-1}$). This result suggests that the Yb ions in YbCr_6Ge_6 possess a Kramers doublet as their ground state at low temperature.

Experimental electronic structure observed by ARPES measurements. To uncover the microscopic origin of the enhanced magnetic and electronic correlations in YbCr_6Ge_6 and to directly probe the interplay between the Cr-derived kagome bands and the Yb-4 f states, we performed systematic ARPES measurements on both surface terminations of YbCr_6Ge_6 and compared them with isostructural LuCr_6Ge_6 . Figures 3a and 3b display the Fermi surfaces (FSs) and core-level spectra obtained from the Cr- and YbGe-terminated surfaces. Although the two terminations exhibit similar FS topology, their spectral intensities differ substantially due to the much larger

DOS contributed by Yb-4*f* electrons near E_F on the YbGe termination. The two terminations can be unambiguously identified from their core-level spectra. On the Cr-terminated surface, the peaks derived from Yb-4*f* states are relatively simple and weak. In contrast, on the YbGe-terminated surface, multiple well-separated 4*f* peaks originating from different Yb layers are observed around -12 to -5 eV, as well as from -2 eV up to E_F , consistent with previous reports ^{20,21}.

Over a wide binding-energy range shown in Fig. 3c, the canonical kagome features (Fig. 3d) previously reported in YCr₆Ge₆ ²² are visible on the Cr termination, together with FBs near E_F and at -1.31 eV, the latter corresponding to the Yb 4*f*_{7/2} state. In contrast, on the YbGe termination, four nearly equally energy-spaced (\sim 0.66 eV) 4*f*-derived FBs are clearly resolved in both the intensity maps and the integrated energy distribution curves (EDCs), and these FBs intersect the kagome-derived conduction bands. When resonant photoemission measurements are performed using 186 eV photons corresponding to the Yb 4*d*–4*f* resonance, the four main FBs (the red solid lines) are significantly enhanced, and an additional set of three weak, nearly equally spaced sub-FBs (the blue dashed lines) emerges at energies midway between the main FBs. These weaker features likely originate from Yb atoms occupying different crystallographic environments in the sample ²³. Figure 3e compares the terminated-dependent band dispersions along the $\bar{\Gamma}$ – \bar{K} direction of YbCr₆Ge₆ with those of LuCr₆Ge₆. The Cr-terminated band structure of YbCr₆Ge₆ is nearly identical to that of LuCr₆Ge₆, except for the presence of an additional FB around -1.31 eV derived from the Yb 4*f*_{7/2} state. In contrast, the YbGe-terminated surface exhibits clear crossings between the 4*f*-derived FBs and the kagome conduction band, giving rise to pronounced *c*–*f* hybridized states, as schematically illustrated in Fig. 3f, which constitute a hallmark of Kondo hybridization.

To directly resolve the $c-f$ hybridization and examine its temperature evolution, we performed temperature-dependent ARPES measurements along the $\bar{M}-\bar{\Gamma}-\bar{M}$ direction on the $k_z \sim 0$ plane of the YbGe-terminated surface, where the band-crossing features are more clearly resolved than along the $\bar{K}-\bar{\Gamma}-\bar{K}$ direction. Figure 4a presents the spectra measured at 150 K and 20 K. At low temperature, all four $4f$ -derived FBs sharpen markedly, and hybridization gaps open at their crossings with the conduction band near -0.3 eV and -0.6 eV below E_F , as highlighted by the red rectangles, which is clearly distinct from that at 150 K, as well as from that of LuCr_6Ge_6 shown in Fig. 4b. A zoomed-in view of the near- E_F region at 150, 115, 85, and 20 K is presented in Fig. 4c, where the hybridization feature near E_F and -0.3 eV becomes prominent at low temperature, as further corroborated by the enlarged images and EDCs in Fig. 4d.

To quantitatively track the temperature dependence of these features, we extracted EDCs at three representative momentum positions (blue square, triangle, and circle in Fig. 4c) and fitted them using a polynomial background combined with Lorentzian peak functions. At the square position, the peak 1 near E_F remains essentially temperature independent, whereas the peak 2 near -0.3 eV shifts upward toward E_F with increasing temperature, demonstrating that the hybridization gap closes at approximately 120 K. This characteristic temperature is higher than the Kondo coherence temperature inferred from transport measurements (Fig. 1f), a behavior commonly observed in Kondo lattice systems. At the triangle position, the EDC peak 3 near E_F exhibit negligible temperature dependence, consistent with the kagome-derived conduction band being largely insensitive to temperature. At the circle position, the EDC peak 4 gradually move toward E_F upon warming, following the same trend as the -0.3 eV peak 2 at the square position and confirming

their origin in the $4f$ -derived states. At high temperatures, the $4f$ -derived hybridized bands near E_F lose coherence and eventually vanish, leaving behind a faint shadow of the kagome FB similar to that observed in YCr_6Ge_6 ²². Because the fitting procedure explicitly accounts for thermal broadening, the observed peak shifts reflect genuine changes in the electronic structure rather than trivial thermal effects. In addition, the temperature evolution of peak 2 and peak 4 exhibits a noticeable kink around 70 – 85 K, consistent with the Kondo coherence temperature inferred from transport measurements (Fig. 1f).

Discussion

When compared to YbV_6Sn_6 ($T_N \sim 0.4$ K)¹⁸, the T_N of YbCr_6Ge_6 is significantly enhanced (~ 3 K). It implies that the existence of local moments of Cr ions in kagome plane compared to the non-magnetic V ions may have some influence on long-range ordering of Yb- $4f$ electrons. On the other hand, the existence of Cr-kagome FB dramatically increases the DOS near E_F , $N(E_F)$. According to the Ruderman-Kittel-Kasuya-Yosida (RKKY) theory, the large $N(E_F)$ serves as a highly efficient medium for the exchange interaction, naturally leading to a much stronger magnetic coupling and a significant enhancement of T_N . The coexistence and interplay of these two types of FBs—one lattice-geometry-driven and one electron-correlation-driven—provide a natural microscopic explanation for the synergistic enhancement of magnetic and electronic correlations revealed by the transport measurements.

In summary, we demonstrate that YbCr_6Ge_6 with Cr kagome lattice exhibit HF features

of Yb-4*f* electrons with the ground state of AFM order below $T_N = 3$ K. Further experimental results reveal that YbCr_6Ge_6 hosts two distinct yet cooperative FB components: a kagome-geometry-imposed one arising from destructive interference in the Cr kagome lattice, and an electron-correlation-driven Yb-4*f* FB associated with Kondo hybridization at low temperature. Present study establishes a new class of quantum states of matter where topological band structure and strong *f*-electron correlations can be studied in synergy. It opens a new frontier for exploring correlated topological phenomena and quantum critical behaviors.

Methods

Single crystal growth. The single crystals of YbCr_6Ge_6 and LuCr_6Ge_6 were grown by using Sn-flux methods. The starting materials Yb (stick, 99.99%), Lu (stick, 99.99 %), Cr (pieces, 99.9999 %), Ge (pieces, 99.999 %) and Sn (grains, 99.999 %) with the molar ratios Yb : Cr : Ge : Sn = 1.5 : 1.167 : 6 : 20 and Lu : Cr : Ge : Sn = 1 : 3 : 6 : 20 were mixed and placed in a corundum Canfield crucible set, which is effective at preventing samples from contacting the silica wool, and then sealed in a quartz tube with backfilled Ar gas (~ 150 Torr). The sealed quartz tube was put into a box furnace and heated to 1323 K in 24 h. After keeping at 1323 K for 10 h, the quartz tube was rapidly cooled at a rate of 5 K/h to 1223 K in order to prevent phase change of quartz tube. Then, it was cooled down to 973 K at 2.5 K/h and the Sn flux is removed by centrifugation. The shiny crystals with typical size about $1 \times 1 \times 0.1$ mm³ can be obtained. The samples were soaked in hydrochloric acid for a short time to remove residual Sn flux on the surface.

Structural and composition characterizations. X-ray diffraction (XRD) patterns of YbCr_6Ge_6

and LuCr_6Ge_6 were measured using a Bruker D8 X-ray diffractometer with $\text{Cu } \kappa_\alpha$ ($\lambda = 1.5418 \text{ \AA}$) radiation at room temperature. The elemental analysis was performed using an energy-dispersive X-ray spectroscopy (EDX) analysis in a FEI Nano 450 scanning electron microscope.

Physical properties measurements. Magnetization measurements were performed using Quantum Design magnetic property measurement system (MPMS3). Electrical transport and heat capacity measurements were performed using physical property measurement system (PPMS-14T). Electrical transport measurements were conducted using a standard four-probe configuration with the current parallel to the ab plane and magnetic field along the c axis.

Angle-resolved photoemission spectroscopy (ARPES) measurements. The ARPES measurements were conducted over a wide range of photon energies at the 03U and 09U endstations of the Shanghai Synchrotron Radiation Facility (SSRF). The μ -ARPES setup featured a beam size smaller than $20 \times 20 \mu\text{m}^2$. The energy and momentum resolutions were maintained at better than approximately 20 meV and 0.02 \AA^{-1} , respectively. Samples smaller than $1 \times 1 \text{ mm}^2$ were cleaved in situ to produce flat, mirror-like $(00l)$ surfaces. During temperature-dependent measurements, the pressure was maintained at a level below 2×10^{-10} Torr.

References

1. Checkelsky, J. G., Bernevig, B. A., Coleman, P., Si, Q. & Paschen, S. Flat bands, strange metals and the Kondo effect. *Nat. Rev. Mater.* **9**, 509–526 (2024).
2. Mielke, A. Ferromagnetism in the Hubbard model on line graphs and further considerations.

J. Phys. A: Math. Gen. **24**, 3311 (1991).

3. Ko, W.-H., Lee, P. A. & Wen, X.-G. Doped kagome system as exotic superconductor. *Phys. Rev. B* **79**, 214502 (2009).
4. Tang, E., Mei, J.-W. & Wen, X.-G. High-Temperature Fractional Quantum Hall States. *Phys. Rev. Lett.* **106**, 236802 (2011).
5. Yin, J.-X., Lian, B. & Hasan, M. Z. Topological kagome magnets and superconductors. *Nature* **612**, 647–657 (2022).
6. Ye, L. et al. Massive Dirac fermions in a ferromagnetic kagome metal. *Nature* **555**, 638–642 (2018).
7. Liu, Z. et al. Orbital-selective Dirac fermions and extremely flat bands in frustrated kagome-lattice metal CoSn. *Nat. Commun.* **11**, 4002 (2020).
8. Ortiz, B. R. et al. CsV₃Sb₅: A Z₂ Topological Kagome Metal with a Superconducting Ground State. *Phys. Rev. Lett.* **125**, 247002 (2020).
9. Ortiz, B. R. et al. Superconductivity in the Z₂ kagome metal KV₃Sb₅. *Phys. Rev. Mater.* **5**, 034801 (2021).
10. Yin, Q. et al. Superconductivity and Normal-State Properties of Kagome Metal RbV₃Sb₅ Single Crystals. *Chin. Phys. Lett.* **38**, 037403–037403 (2021).
11. Yin, J.-X. et al. Quantum-limit Chern topological magnetism in TbMn₆Sn₆. *Nature* **583**, 533–536 (2020).

12. Wang, Q. et al. Field-induced topological Hall effect and double-fan spin structure with a c -axis component in the metallic kagome antiferromagnetic compound YMn_6Sn_6 . *Phys. Rev. B* **103**, 014416 (2021).
13. Li, M. et al. Dirac cone, flat band and saddle point in kagome magnet YMn_6Sn_6 . *Nat. Commun.* **12**, 3129 (2021).
14. Arachchige, H. W. S. et al. Charge Density Wave in Kagome Lattice Intermetallic ScV_6Sn_6 . *Phys. Rev. Lett.* **129**, 216402 (2022).
15. Wirth, S. & Steglich, F. Exploring heavy fermions from macroscopic to microscopic length scales. *Nat. Rev. Mater.* **1**, 16051 (2016).
16. Shim, J. H., Haule, K. & Kotliar, G. Modeling the Localized-to-Itinerant Electronic Transition in the Heavy Fermion System CeIrIn_5 . *Science* **318**, 1615–1617 (2007).
17. Chen, Q. Y. et al. Direct observation of how the heavy-fermion state develops in CeCoIn_5 . *Phys. Rev. B* **96**, 045107 (2017).
18. Guo, K., Ye, J., Guan, S. & Jia, S. Triangular Kondo lattice in YbV_6Sn_6 and its quantum critical behavior in a magnetic field. *Phys. Rev. B* **107**, 205151 (2023).
19. Romaka, V. et al. Structure, bonding, and properties of RCr_6Ge_6 intermetallics (R = Gd–Lu). *J. Solid State Chem.* **338**, 124874 (2024).
20. Kummer, K. et al. Intermediate valence in Yb compounds probed by 4f photoemission and resonant inelastic x-ray scattering. *Phys. Rev. B* **84**, 245114 (2011).

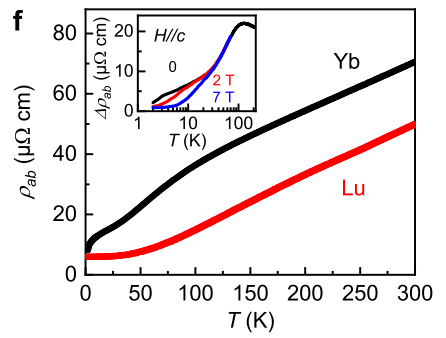
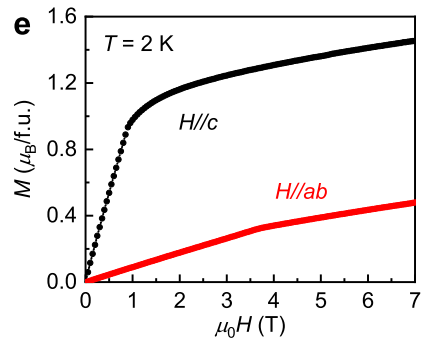
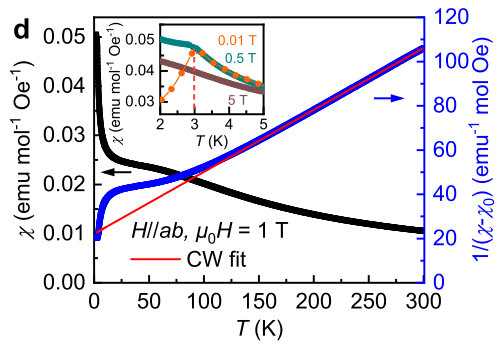
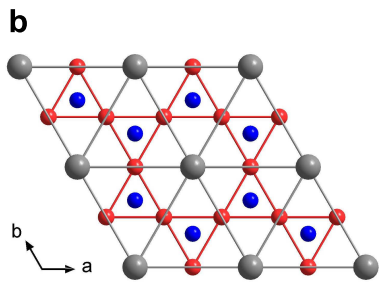
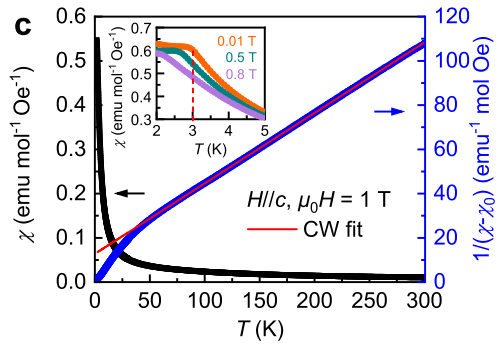
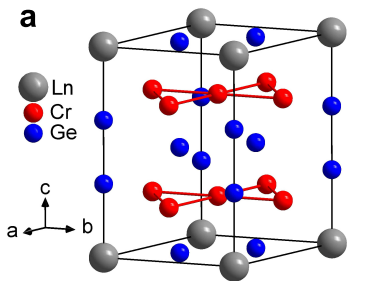
21. Lou, R. et al. Strongly Entangled Kondo and Kagome Lattices and the Emergent Magnetic Ground State in Heavy-Fermion Kagome Metal YbV_6Sn_6 . *Phys. Rev. Lett.* **135**, 146902 (2025).
22. Yang, T. Y. et al. Fermi-level flat band in a kagome magnet. *Quantum Frontiers* **1**, 14 (2022).
23. Weiland, A. et al. Refine Intervention: Characterizing Disordered $\text{Y}_{0.5}\text{Co}_3\text{Ge}_3$. *Cryst. Growth Des.* **20**, 6715–6721 (2020).

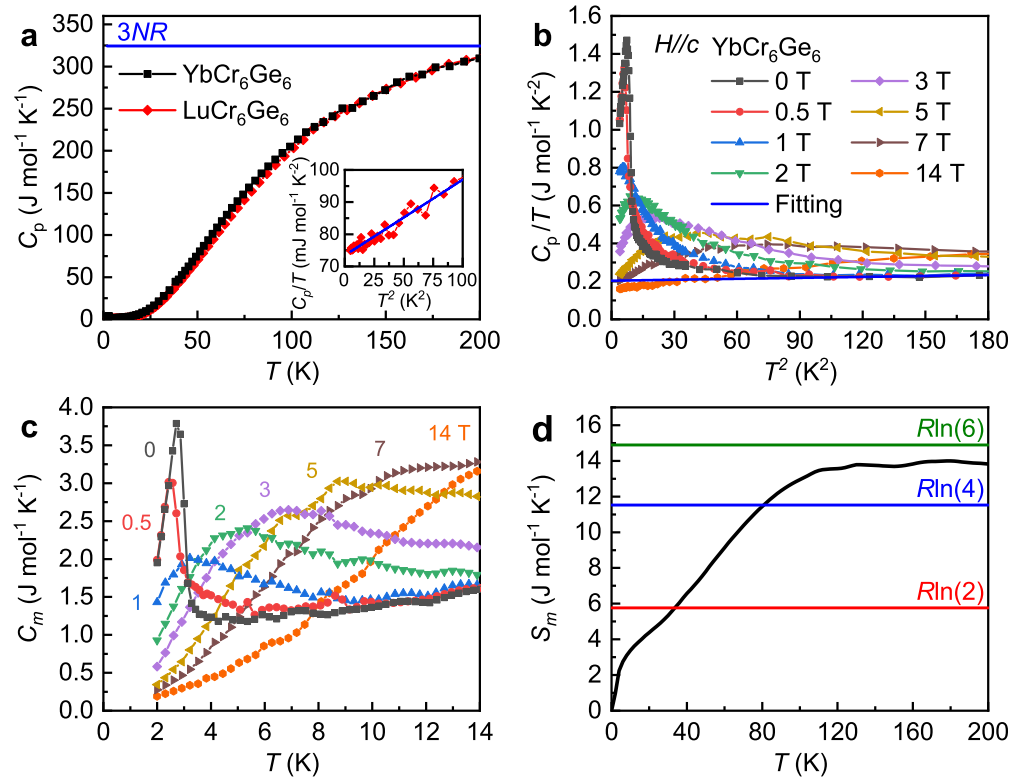
Acknowledgements This work is supported by the National Key R&D Program of China (Grant Nos. 2022YFA1403800 and 2023YFA1406500), the National Natural Science Foundation of China (Grant Nos. 12274459 and 12222413), the Natural Science Foundation of Shanghai (Grants No. 23ZR1482200), and the Natural Science Foundation of Ningbo (Grants No. 2024J019), the Innovation Yongjiang 2035 Key R&D Programme-International Sci-tech Cooperation Projects, the funding of Ningbo Yongjiang Talent Program and the Mechanics Interdisciplinary Fund for Outstanding Young Scholars of Ningbo University (Grants No. LJ2024003). We thank the SSRF of BL03U (31124.02.SSRF.BL03U) for the assistance with ARPES measurements.

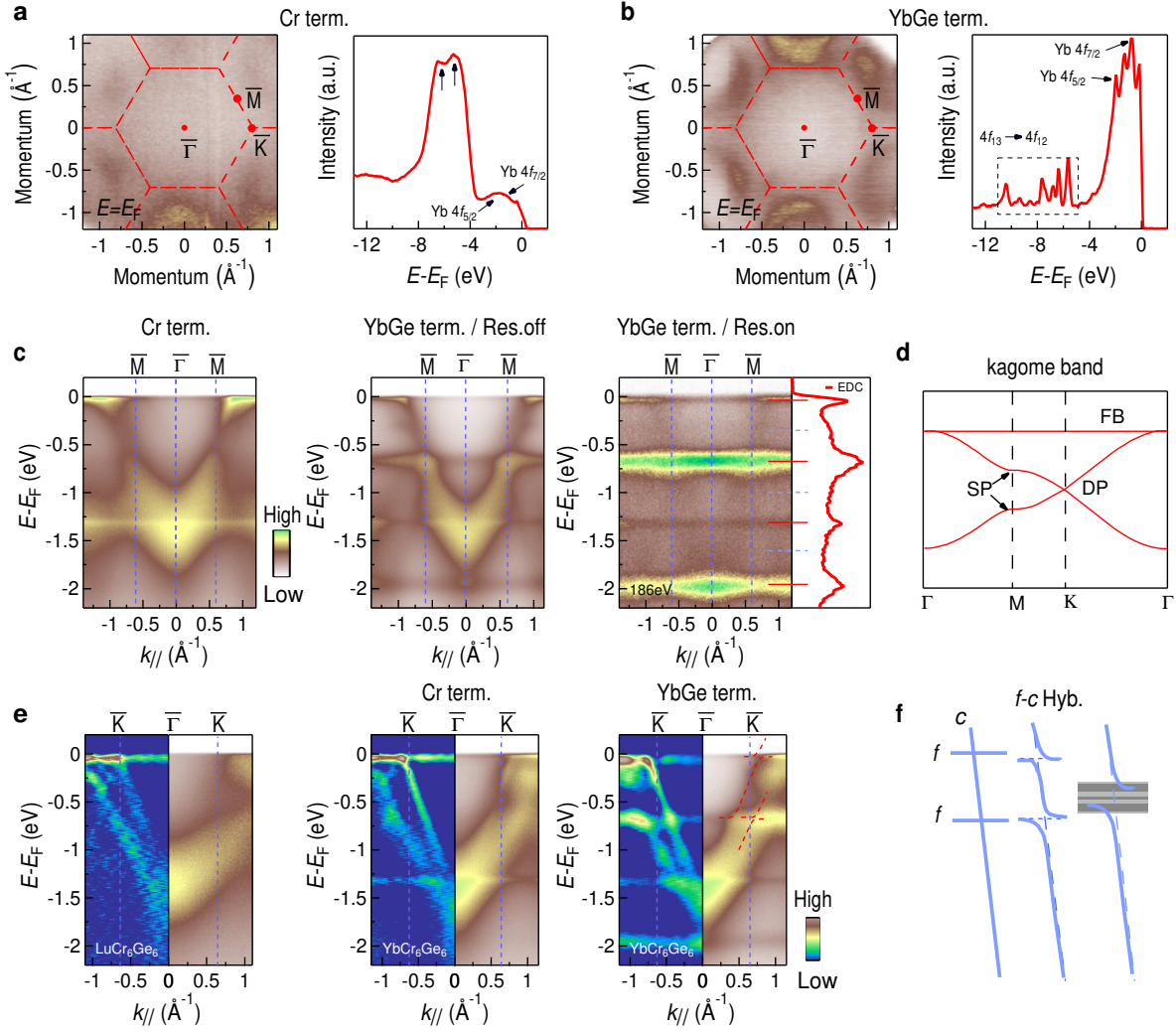
Author contributions H.C.L., provided strategy and advice for the research; W.X.L., S.J. T. and Y. M. performed the crystal growth, structural and physical properties characterizations and fundamental data analysis with the assistance of S.G.W., X.Z., and H.C.L.; P.C.M., T.Q.W. and Z.H.L. performed the ARPES measurements and analyzed the data; H.C.L., Z.H.L. and W.X.L. wrote the manuscript based on discussion with all the authors.

Supplementary Information accompanies this paper.

Author Information The authors declare no competing financial interests. The data that support the findings of this study are available from the corresponding author H.C.L. (hlei@ruc.edu.cn) upon reasonable request.







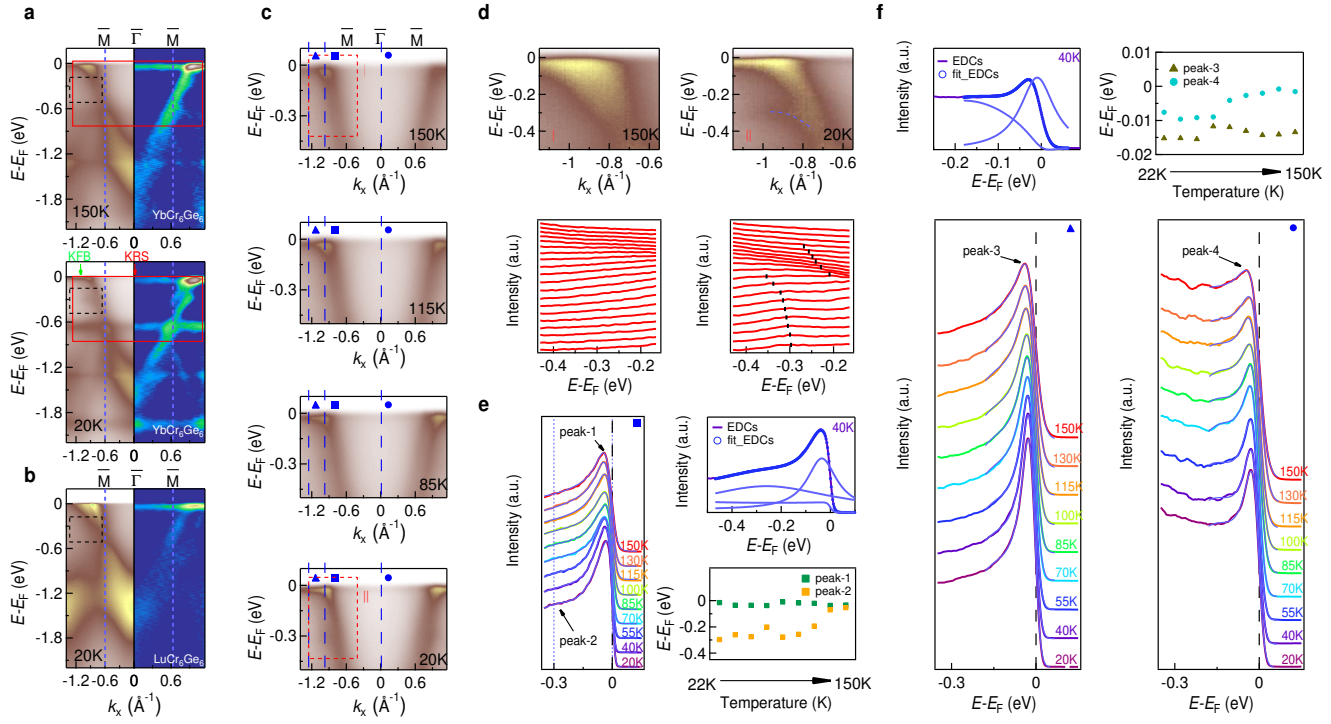


Figure 1 Crystal structure, magnetization and resistivity of LnCr_6Ge_6 single crystals. **a**, Crystal structure of LnCr_6Ge_6 . The big gray, medium red and small blue balls represent Ln, Cr and Ge atoms, respectively. **b**, Top view of LnCr_6Ge_6 crystal structure to highlight the Ln triangle lattice and Cr kagome lattice. **c** and **d**, Temperature dependence of $\chi(T)$ (left axis) and $(\chi(T) - \chi_0)^{-1}$ (right axis) of YbCr_6Ge_6 single crystal at $\mu_0H = 1$ T for $H \parallel c$ and $H \parallel ab$, respectively. The red solid lines represent the fits using the CW law at high-temperature region. Insets: $\chi(T)$ curves at various fields around T_N . **e**, Field dependence of $M(\mu_0H)$ at $T = 2$ K for both $H \parallel c$ (black symbols) and $H \parallel ab$ (red symbols). **f**, zero-field $\rho_{ab}(T)$ as a function of temperature for YbCr_6Ge_6 and LuCr_6Ge_6 single crystals. Inset: $\Delta\rho_{ab}$ vs T for YbCr_6Ge_6 from 1.8 K to 120 K at $\mu_0H = 0, 2$ and 7 T.

Figure 2 Specific heat and magnetic entropy. **a**, Temperature dependence of zero-field specific heat $C_p(T)$ between 2 K and 200 K for YbCr_6Ge_6 (black) and LuCr_6Ge_6 (red). Inset shows the linear fit of C_p/T vs. T^2 for LuCr_6Ge_6 . **b**, Low-temperature C_p/T of YbCr_6Ge_6 as a function of T^2 in different magnetic fields for $H \parallel c$. **c**, Low-temperature magnetic specific heat $C_m(T)$ of YbCr_6Ge_6 in various magnetic fields, after subtracting the specific heat of LuCr_6Ge_6 . **d**, Magnetic entropy $S_m(T)$ of YbCr_6Ge_6 in zero field.

Figure 3 Termination-dependent Fermi surfaces and low-energy electronic structure. **a** and **b**, Fermi surface maps and corresponding core-level spectra measured on the Cr- and YbGe-terminated surfaces of YbCr_6Ge_6 , respectively. The red frames denote

the 2D Brillouin zone projected onto the (001) plane. All data were acquired using a photon energy of 92 eV (corresponding to the $k_z \sim 0$ plane), unless otherwise specified. **c**, ARPES intensity plots along the $\bar{\Gamma}-\bar{M}$ direction for the two surface terminations. The data shown in the right panel were taken using 186 eV photons, corresponding to the Yb 4d–4f resonant photoemission condition. The integrated EDC reveals nearly equally energy-spaced 4f-derived peaks. **d**, Representative kagome band structure obtained from a tight-binding calculation, highlighting the flat bands, saddle points, and Dirac points. **e**, ARPES intensity plots and corresponding second-derivative maps along the $\bar{\Gamma}-\bar{K}$ direction for LuCr_6Ge_6 and for the two surface terminations of YbCr_6Ge_6 . **f**, Schematic illustration of the hybridization between the conduction band and the localized Yb-4f bands.

Figure 4 Temperature-dependent evolution of the flat bands. **a**, ARPES intensity plots and corresponding second-derivative maps along the $\bar{\Gamma}-\bar{M}$ direction on the $k_z \sim 0$ plane for the YbGe-terminated surface of YbCr_6Ge_6 , acquired at 150 K and 20 K, respectively. The green markers labeled KFB denote the kagome FBs, while the red markers labeled KRS indicate the Kondo resonance state. **b**, The same measurements as in **a**, but performed on LuCr_6Ge_6 at 20 K. **c**, ARPES intensity plots of the enlarged regions in **a**, measured at 150 K, 115 K, 85 K, and 20 K, respectively. **d**, Enlarged views of the red dashed boxes in **c** at 150 K and 20 K, highlighting clear temperature-induced changes. The corresponding EDCs are shown below. **e**, Temperature evolution of EDCs at the momentum positions marked by the blue square in **c**. The EDCs are fitted using a polynomial background and Lorentzian functions. The extracted peak positions are summarized in

the right panels, where the size of the squares represents the maximum fitting uncertainty.

f, Same analysis as in **e**, but for the momentum positions indicated by the blue triangle and blue circle in **c**.